

Synthesis of hexagonal boron arsenide nanosheets for low-power consumption flexible memristors

Received: 22 January 2025

Accepted: 12 May 2025

Published online: 22 May 2025

 Check for updates

Zenghui Wu¹, Yuxuan Zhang¹, Boxiang Gao¹, You Meng¹, He Shao¹, Dengji Li¹, Pengshan Xie¹, Weijun Wang¹, Bowen Li^{1,2}, Chenxu Zhang^{1,3}, Yi Shen¹, Di Yin¹, Dong Chen¹, Quan Quan¹, SenPo Yip⁴ & Johnny C. Ho^{1,2,4,5} ✉

Boron arsenide has recently attracted significant attention for its thermal and electronic properties. However, its lengthy growth process and bulk structure limit its application in advanced semiconductor systems. In this study, we introduce a method for synthesizing ultrathin crystalline hexagonal boron arsenide (h-BAs) nanosheets in large quantities via an in-situ chemical reaction of sodium borohydride with elemental arsenic in a low-pressure hydrogen atmosphere. We successfully fabricated h-BAs-based memory devices with ON/OFF current ratios up to 10^9 , low energy consumption of less than 4.65 pJ, and commendable stability. Furthermore, we have developed flexible h-BAs-based memristors with good stability and robustness. This research not only provides a promising avenue for synthesizing h-BAs nanosheets, but also underscores their potential in the development of next-generation electronic devices.

Boron arsenide (BAs), the least studied III-V semiconductor due to the challenges in growing high-quality crystals, has recently drawn significant research interest. This is attributed to its remarkable properties, including ultrahigh thermal conductivity ($1300 \text{ W m}^{-1} \text{ K}^{-1}$) and unusual carrier mobility (electron: $1400 \text{ cm}^2 \text{ V}^{-1} \text{ s}^{-1}$; hole: $2110 \text{ cm}^2 \text{ V}^{-1} \text{ s}^{-1}$), as indicated by both theoretical predictions and experimental synthesis^{1–7}. Notably, two-dimensional (2D) hexagonal boron arsenides (h-BAs) are theoretically predicted to exhibit good thermal transport properties, high carrier mobility, and strain-tunable electronic properties^{8–10}. This unique combination of attributes makes BAs a promising candidate for next-generation optoelectronic, photovoltaic, and thermoelectric applications^{5,11}. However, despite these promising theoretical predictions, the experimental observation of h-BAs and their subsequent application in devices remain unreported.

In fact, the synthesis of BAs is notably challenging due to several factors: the high volatility and vapor pressure of arsenic, the high melting point of boron ($-2076 \text{ }^\circ\text{C}$), and the potential formation of

amorphous or sub-crystalline phases (such as B_{12}As_2) at elevated temperatures. These complexities hinder the preparation of high-quality BAs crystals, limiting research in this area¹. With its unique electronic configuration ($[\text{He}]2s^22p^1$), boron shares properties with carbon, forming a vast array of structures, including linear chains, extended 2D sheets of borophene, and space-filling B_{12} icosahedra¹². This versatility allows boron to incorporate with other elements for numerous chemical combinations¹³. Interestingly, the temperature required to synthesize borophene using sodium borohydride ($600 \text{ }^\circ\text{C}$) is close to the sublimation temperature of arsenic ($615 \text{ }^\circ\text{C}$)¹⁴, suggesting a viable experimental approach for preparing BAs. This insight opens promising avenues for exploring and potentially overcoming the synthesis challenges of BAs.

Here, we have successfully synthesized large-scale, ultrathin hexagonal boron arsenide nanosheets (h-BAsNSs) in a hydrogen-rich environment. Utilizing a controlled three-step heating procedure, we achieved in situ thermal decomposition and chemical reactions of

¹Department of Materials Science and Engineering, City University of Hong Kong, Hong Kong SAR, PR China. ²Shenzhen Research Institute, City University of Hong Kong, Shenzhen, PR China. ³State Key Laboratory of Radio Frequency Heterogeneous Integration (Shenzhen University), College of Electronics and Information Engineering, Shenzhen, PR China. ⁴Institute for Materials Chemistry and Engineering, Kyushu University, Fukuoka, Japan. ⁵State Key Laboratory of Terahertz and Millimeter Waves, City University of Hong Kong, Hong Kong SAR, PR China. ✉e-mail: johnnyho@cityu.edu.hk

NaBH_4 and arsenic to grow these nanosheets. The morphologies and crystal structures of the h-BASnSs were carefully characterized using scanning electron microscopy (SEM), atomic force microscopy (AFM), transmission electron microscopy (TEM), and selected-area electron diffraction (SAED). Our findings reveal that h-BAs possess a hexagonal crystal structure with a lattice constant of 3.39 Å, where boron atoms are bonded to four equivalent arsenic atoms, forming corner-sharing BAS_4 tetrahedra. The optical properties of h-BASnSs were examined through Raman spectroscopy, ultraviolet-visible (UV-vis) diffuse reflectance, and infrared spectroscopy. As a proof-of-concept application, we fabricated a non-volatile re-writable memory device using

h-BASnSs as the charge-trapping material and polyvinylpyrrolidone (PVP) as an insulator. These results highlight the promising potential of h-BAs for developing tunable synapses and other advanced device applications.

Results

BAs nanosheets preparation and verification

The experimental setup and synthesis process are schematically depicted in Fig. 1a. Specifically, we developed a typical heating process to synthesize large-scale and free-standing BAs by in situ thermally decomposing NaBH_4 powders and reacting them with arsenic. The

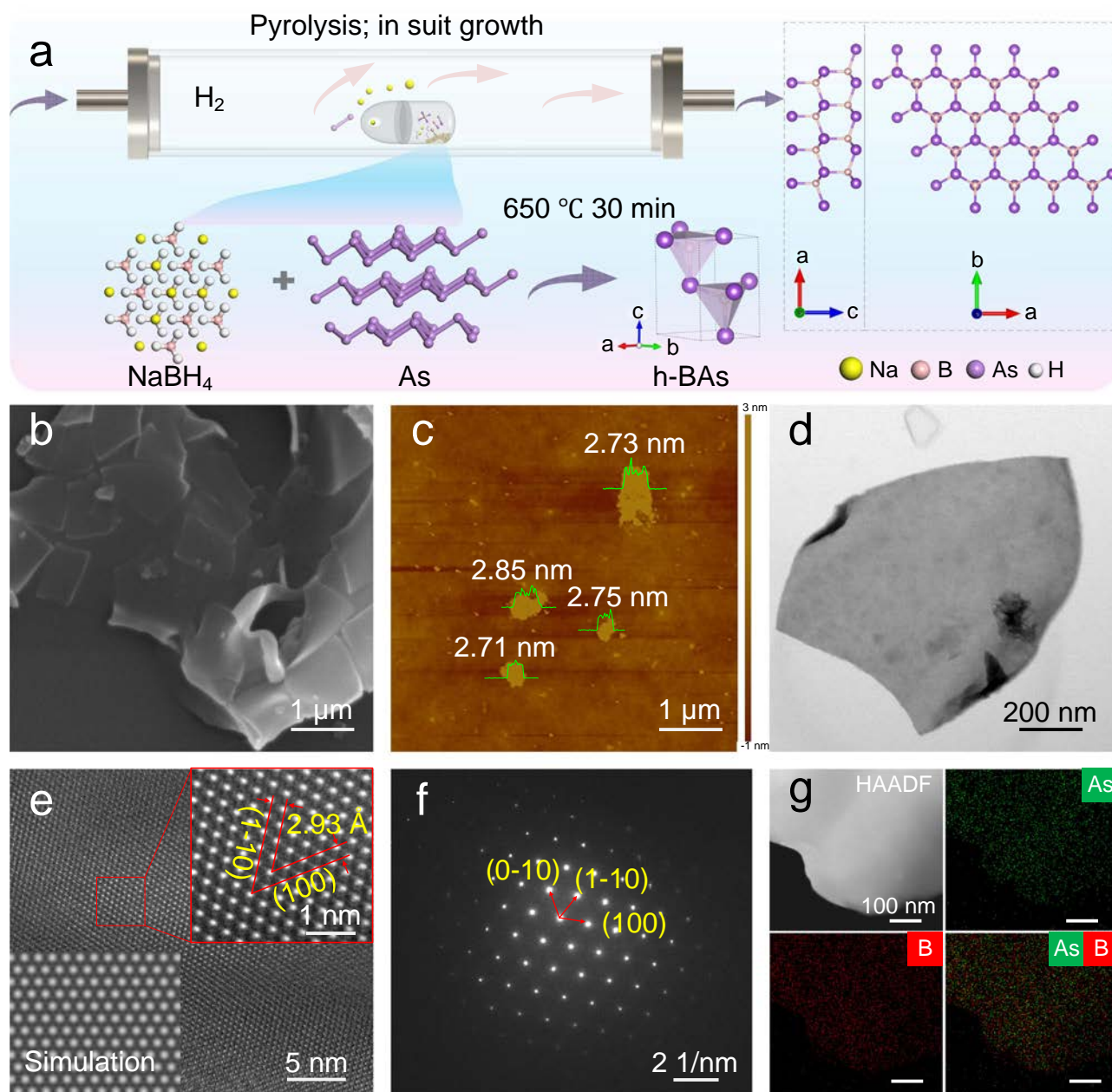


Fig. 1 | Synthesis diagram and morphology characterization of the h-BAS nanosheet. **a** Schematic diagram of the in situ growth of h-BAs. **b** Scanning electron microscopy (SEM) images of h-BAS nanosheets. **c** Atomic force microscopy (AFM) image of the sheets. Height analysis along the green line in the inset indicates a thickness of around 2.7 nm. **d** Low-magnification transmission electron microscopy (TEM) image of a typical h-BAS nanosheet. **e** High-magnification transmission electron microscopy (HRTEM) image of the h-BAS nanosheet. The inset in the upper

right corner is the corresponding fast Fourier-transform pattern of the HRTEM image derived from the red region. The inset in the lower left corner is the HRTEM map extracted from the calculation model. **f** The corresponding selected-area electron diffraction (SAED) pattern image of the h-BAS nanosheet. **g** High-angle annular dark-field-scanning transmission electron microscopy imaging and the accompanying energy-dispersive X-ray spectroscopy elemental mapping (HAADF-STEM-EDS) of a typical h-BAS nanosheet.

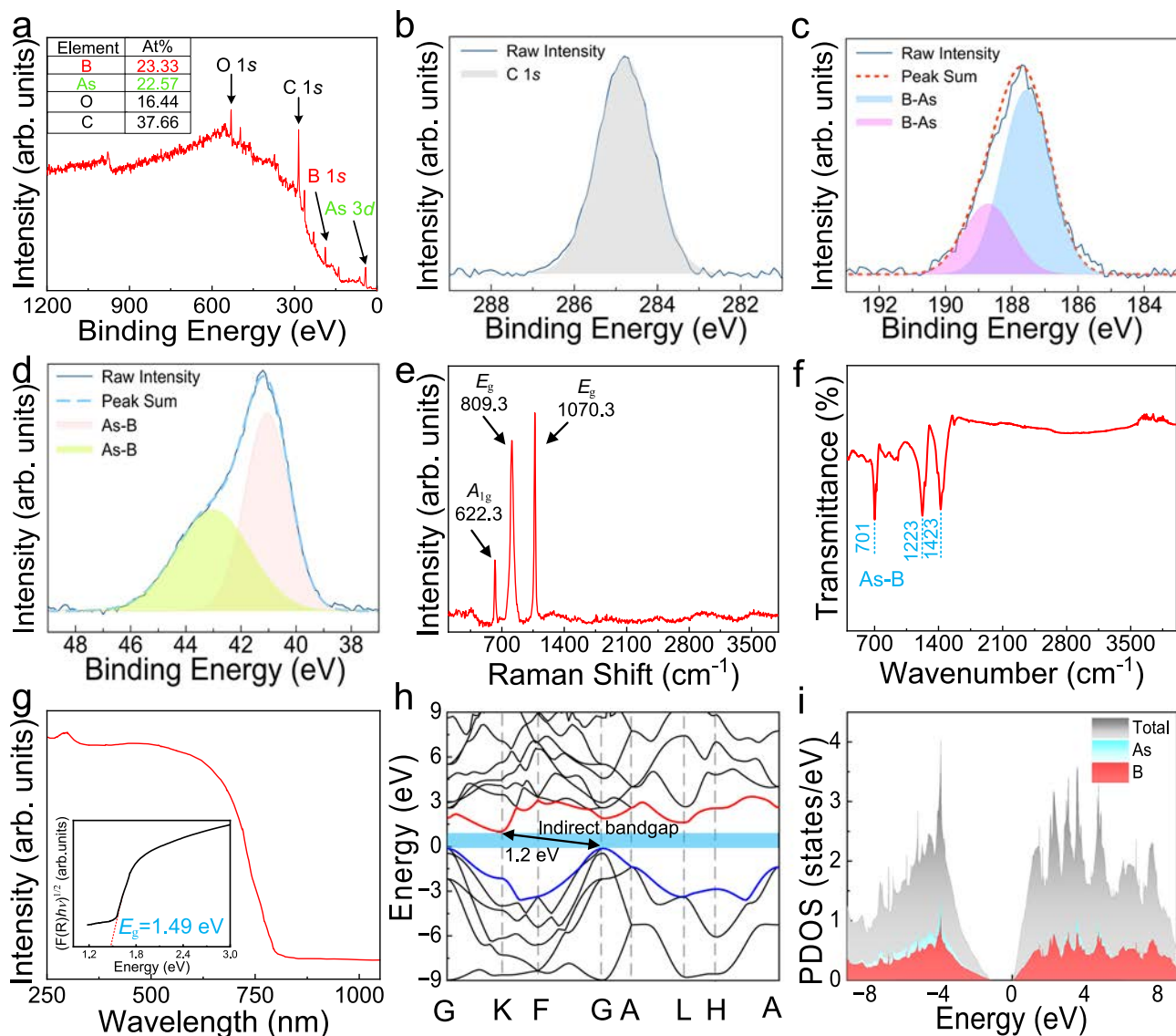


Fig. 2 | Structural and optical properties of the h-BAs nanosheet. **a** Full-scale X-ray photoelectron spectroscopy (XPS) survey of the h-BAs nanosheet. High-resolution spectra of **b** C 1s, **c** B 1s, and **d** As 3d of the h-BAs nanosheet. **e** Raman, **f** infrared (IR) and **g** ultraviolet–visible (UV-vis) diffuse reflectance spectra of the

h-BAs nanosheet (in the inset, the corresponding optical band gap (E_g) is estimated to be 1.49 eV using the Kubelka-Munk function ($F(R)$), by plotting the $(F(R) \cdot hv)^{1/2}$ versus photon energy (hv)). **h** Band gap structure and **i** projected density of states (PDOS) of the h-BAs nanosheet.

mixed powders were heated from room temperature to 650 °C at a programmed temperature rate (Supplementary Fig. 1) and maintained at this temperature for 30 min to produce large-scale h-BAsNSs. The detailed principle will be discussed in the methods section. The nanosheet is a few-layer hexagonal wurtzite structure that features h-BAs cells with a 4-atom unit cell ($a = 3.39 \text{ \AA}$) (Fig. 1a). The sample was then centrifuged and purified for further characterization. The corresponding SEM images of the h-BAs nanosheets are shown in Fig. 1b, which reveals the irregularly shaped structure of the h-BAsNSs by the purification process. AFM was employed to further characterize the thickness and lateral size of the sheets (Fig. 1c). The results show that the thickness of a typical sheet is close to 2.75 nm. The low-magnification TEM image shows that one h-BAsNS is irregular but ultrathin (Fig. 1d), which is well consistent with the AFM image (Fig. 1c). The high-magnification transmission electron microscopy (HRTEM) image of h-BAsNSs derived from one typical region in Fig. 1d and the corresponding SAED pattern show that the h-BAsNS is crystalline (Fig. 1e, f). The measured interplanar crystal spacings are around 2.93 Å, which can be ascribed to the ($\bar{1}10$) and (100) planes of h-BAs

crystal, respectively (Fig. 1a). Moreover, the chemical composition of the obtained h-BAsNS was confirmed by energy-dispersive X-ray spectroscopy (EDS) mapping. The elemental ratio of boron and arsenic is around 1:1, as shown in Supplementary Fig. 2, which is close to the predicted h-BAs. High-angle annular dark-field (HAADF) images of the h-BAsNSs were recorded in different positions of the sample using a scanning transmission electron microscope (STEM), as depicted in Fig. 1g. A typical h-BAsNS is shown in the HAADF image (Fig. 1g). The mapping images show that boron (B) and arsenic (As) elements are uniformly distributed in the nanosheets without aggregation. These results further confirm that h-BAsNSs have been successfully realized through the controlled thermal process.

The chemical bonding of h-BAsNS was investigated by X-ray photoelectron spectroscopy (XPS), as displayed in Fig. 2a–d. To confirm the accuracy of the analysis of the B 1s and As 3d spectra, the C 1s spectrum of the sample was calibrated to 284.8 eV (Fig. 2b). Carbon and oxygen mainly come from the carbon glue used to support the sample. The high-resolution B 1s spectrum is shown in Fig. 2c and features characteristic peaks located at 187.6 and 188.7 eV in the range

reported for boride^{5,15}, indicating two types of B–As bonding, which is consistent with the crystal structure in Fig. 1a. The high-resolution As 3*d* spectrum is displayed in Fig. 2d and presents characteristic peaks at 40.9 and 42.9 eV in the range reported for BAs^{5,15}. It is worth mentioning that the sheets maintained their structural integrity even after exposure to air for over 1 month (Supplementary Fig. 3).

Raman spectroscopy was employed to reveal the remarkable structure and unique electronic and phonon properties of h-BAsNS (Fig. 2e). The results show that the three intense peaks at 622.3, 809.3, and 1070.3 cm⁻¹ can be ascribed to the different modes of the BAs bonds. The Raman spectrum of the h-BAsNS is entirely different from those of the mixed source (Supplementary Fig. 4b) and possible byproducts (Supplementary Fig. 4c–i)^{14,16–19}. Attenuated total reflectance Fourier-transform infrared (ATR-FTIR) spectra were used to determine the structural characteristics of the sheet, as shown in Fig. 2f. Unlike the source or other borides and arsenides (Supplementary Fig. 5), the absorption peaks of the sheets located at 701, 1223, and 1423 cm⁻¹ originate from the BAs stretching vibration of h-BAsNSs. The optical properties of the h-BAsNSs were analyzed by UV-vis diffuse reflectance spectroscopy (Fig. 2g). The UV/Vis spectrum demonstrates that the sheets are semiconducting, and the corresponding optical band gap (E_g) is estimated to be 1.49 eV using the Kubelka-Munk function ($F(R)$), by plotting the $(F(R) \cdot h\nu)^{1/2}$ versus photon energy ($h\nu$). We then further explored the electronic properties of h-BAsNSs using first-principles calculations based on the PBE0 hybrid exchange-correlation functional. It was found that h-BAs is an indirect-band gap semiconductor with a band gap of 1.2 eV between the valence-band maximum and the conduction band minimum (Fig. 2h). The corresponding projected density of states (PDOS) is shown in Fig. 2i. These theoretical results are consistent with the experimental observation within a reasonable deviation range because the first-principles calculations usually underestimate the band gap usually²⁰.

Growth mechanism of h-BAs

To shed light on the growth mechanism of h-BAs, we investigated the effect of the annealing temperature and reaction duration on the resulting products. The reaction time was set at 30 min. When the temperature was below 600 °C, the powder reaction was insufficient. It was difficult to form a substantial number of nanosheets (Supplementary Fig. 6a). Numerous nanosheets started to form at 600 °C (Supplementary Fig. 6b). Still, they were found to be amorphous based on the TEM results (Supplementary Fig. 7a). Once the temperature was increased to 650 °C, large-area nanosheets were formed (Supplementary Fig. 6c), and they were crystalline (Fig. 1b–f). However, when the temperature increased to 700 or 750 °C, the nanosheets were fused into blocks with wrinkled surfaces (Supplementary Fig. 6d, e). At 800 °C, these blocks were etched again by hydrogen to form a secondary nanosheet structure (Supplementary Fig. 6f). Hence, the temperature of 650 °C is suitable for forming good-quality h-BAs. Furthermore, it was also found that some samples are multi-crystalline or amorphous, possibly due to the structural destruction of the h-BAsNSs under high-energy electron irradiation for low-mass boron atoms¹⁴, as shown in Supplementary Fig. 8. The dynamics of forming the sheets were also probed at 650 °C. When the reaction time was 5 min, the powder source did not fully react and decompose, and there were no nanosheets (Supplementary Fig. 9a). For the reaction time of 15 min, some small-area thick amorphous nanosheets that had just been decomposed from the bulk source can be obtained (Supplementary Figs. 7b and 9b). After the reaction time was extended to 30 min, large-area and very thin nanosheets were obtained (Supplementary Fig. 9c). However, extending the reaction time to 60 min or more led to a trend of decomposition and fusion; the nanosheet area became larger, with the nanosheets eventually merging into a network or even thick

wrinkles (Supplementary Fig. 9d–f), and these nanosheets were amorphous (Supplementary Fig. 7b–d). Thus, 30 min at 650 °C is optimal for synthesizing the h-BAs.

To address the easy sublimation of elemental arsenic, we customized a quartz bottle with 1 mm holes to slow the diffusion rate of the reaction source, enabling a complete reaction within the bottle and promoting crystallization (Fig. 3a). The growth temperature and time are significantly lower than those of cubic BAs (>800 °C) or B₁₂As₂ (920 °C), which is mainly attributed to the self-catalyzing growth of the metal Na acting as an in situ gas template produced during the thermal decomposition of NaBH₄¹⁴. To elucidate this process, we present first-principles calculations of sodium borohydride decomposition, which produces free boron and metallic sodium. These calculations detail the breaking of borohydride bonds catalyzed by sodium (Supplementary Fig. 10). Furthermore, the reaction process of boron-arsenic bond formation catalyzed by sodium atoms and the corresponding transition state energies are illustrated in Fig. 3c. Under the catalysis of sodium atoms, B–H bonds are breaking and boron atoms combine with arsenic to form B–As bonds, which lower the local energy of the system, making it more stable. With the formation of numerous boron-arsenic bonds, stable hexagonal BAs crystals are anticipated to emerge. The adsorption of alkali-metal atoms (Li, Na, and K) onto the h-BAs sheet is highly beneficial for activating boron atoms²¹. It may markedly increase the B–As binding energy to form a stable structure similar to the hydrogenated borophene at a certain temperature^{14,22,23}. Generally, the reaction of NaBH₄ and As is summarized as follows^{14,24,25}:



Experimental demonstration and mechanism of the BAs memristor

Apart from understanding the synthesis, it is also essential to investigate the application potential of the h-BAs nanosheets. Following the technical route of organic-inorganic hybrid devices^{26,27}, as a proof-of-concept application, we used PVP polymers as a polymer matrix to mix with h-BAsNSs, referred to as h-BAs-PVP, to fabricate an h-BAs-based memory device on a quartz substrate (Fig. 4a). We employed Ag as a top electrode (TE) and Au as a bottom electrode (BE), respectively, which is similar to other devices, such as those made from phosphene, borophene, and MoS₂^{14,28,29}. This device shows the coexistence of threshold switching (TS) and memory switching (MS) characteristics and engenders expanded opportunities for developing selector and memory devices^{30,31}. In TS mode, the direct-current current–voltage (I – V) sweeps of the device, as shown in Fig. 4b, displayed a bi-directional TS performance for 50 I – V cycles with a current compliance (I_{CC}) limit of 100 μA. The initial voltage was swept from 0 to +1V, dramatically increasing the current from 6.4×10^{-14} to 1×10^{-4} A at a positive threshold voltage (V_{th+}) of 0.425 V. Notably, the device remained in the low-resistance state (LRS) within a voltage range from +1 to 0 V, but it returned to the initial turn-off state during the operation interval of positive and negative voltage sweep. It is worth noting that when a negative voltage sweep (0 V → -1 V → 0 V) with the same I_{CC} was applied, a TS loop was almost symmetric to the positive one. The V_{th+} (-0.47 ± 0.03 V) and negative threshold voltage (V_{th-}) (0.45 ± 0.02) distribution in the h-BAs memristor is relatively narrow, as depicted in Supplementary Fig. 11a, b. In MS mode, repeatable

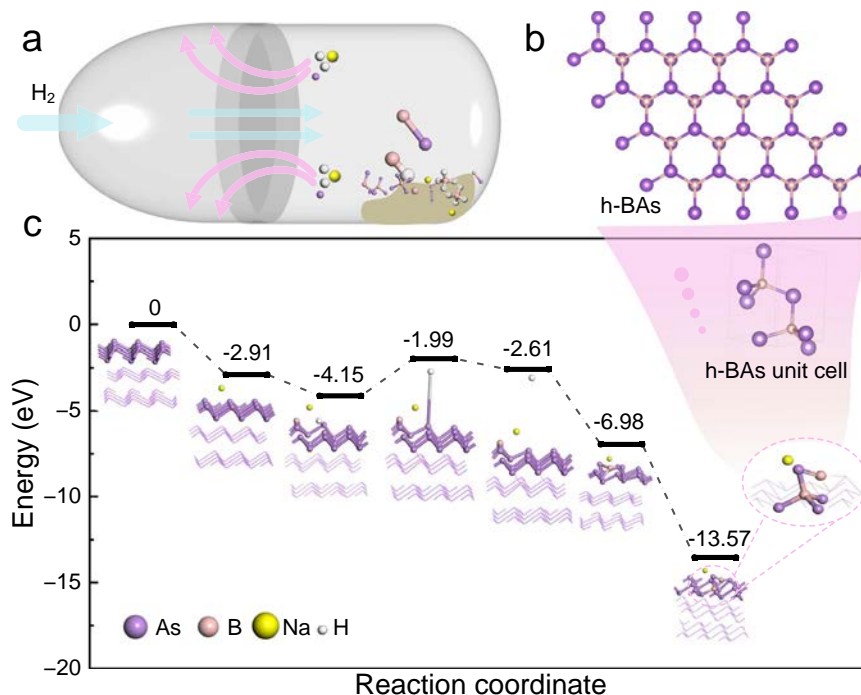


Fig. 3 | The growth mechanism of h-BAs. a Homemade quartz bottle for the reaction of easily sublimable arsenic elements. **b** Top view of the h-BAs crystal structure and **c** Reaction pathway of BAs over the Na catalyst.

bipolar memristive switching I - V curves during five cycles were shown in Fig. 4c. The initial voltage was swept from 0 to +1 V, dramatically increasing the current from 2.23×10^{-13} to 1×10^{-4} A at a positive set voltage (V_{set}) of 0.43 V (Step 1). This transition from the high-resistance state (HRS, OFF state) to the LRS was akin to a writing process in digital memory devices. The ultra-low standby power ($P_{\text{Standby}} = I_{\text{HRS}} \times V_{\text{set}}$) of -95.9 fW was achieved, which is desirable for low leakage current and cell disturbance memristors. Notably, the device remained in the LRS within a voltage range from +1 to 0 V (Step 2) and remained in the LRS state when the negative voltage was swept from 0 to -1 V (Step 3). A transition from the LRS back to the HRS occurred at a V_{reset} of -0.39 V (Step 4), equivalent to the erasing process of digital memory. The subsequent positive and negative sweeps suggest that the device could be rewritten and re-erased, indicating a promising potential of h-BAs for advanced memory devices. The memristor shows non-volatile switching from a compliance current of 1 pA (Supplementary Fig. 11c), and the power consumption during the set on transition (P_{set}) is very low, that is, $P_{\text{set}} = I_{\text{LRS}} V_{\text{set}} = 1 \text{ pA} \times 0.44 \text{ V} = 440 \text{ fW}$, where I_{LRS} corresponds to the I_{CC} used in this experiment. Further measurements of the device's performance and stability were performed using rectangular voltage pulses via a recommended process³². The single pulse sequence of read (0.2 V, 1 μ s), set (1 V, 1 μ s), read (0.2 V, 1 μ s), reset (-1 V, 1 μ s), and read (0.2 V, 1 μ s) was applied to the Ag/h-BAs-PVP/Au device. The device shows short switching time (t) and low switching energy (E); these values can be pushed down to $t_{\text{set}} = 300 \text{ ns}$, $t_{\text{reset}} = 200 \text{ ns}$, $E_{\text{set}} = I_{\text{LRS}} V_{\text{set}} t_{\text{set}} = 77.5 \text{ } \mu\text{A} \times 0.2 \text{ V} \times 300 \text{ ns} = 4.65 \text{ pJ}$ and $E_{\text{reset}} = I_{\text{LRS}} V_{\text{set}} t_{\text{set}} = 66.7 \text{ } \mu\text{A} \times 0.2 \text{ V} \times 200 \text{ ns} = 2.67 \text{ pJ}$ (Supplementary Fig. 11d). The reasons behind these observations are the high conductivity and diffusivity of Ag^+ ions^{33,34}. The endurance of the devices was tested at set pulses of 1 V and reset pulses of -1 V. The sequence of the cycles was: set (1 V, 2 ms), read (0.2 V, 2 ms), reset (-1 V, 2 ms), and read (0.2 V, 2 ms). The interval between each pulse is 2 ms. In these experiments, we demonstrated endurance better than 5000 cycles without obvious degeneration of the ON and OFF states (see Fig. 4d). Figure 4e illustrates an ample separation between the LRS and the HRS within a 0.2 V operating voltage, from which a high on/off ratio of $>10^9$

could be obtained, revealing promising data-saving capability through the retention time test.

To further reveal the switching mechanism of the h-BAs-based device, typical I - V MS characteristics were assessed, as shown in Fig. 4f. In the OFF state (Region A), the plot of $\ln(I)$ vs. $V^{1/2}$ from 0 to 0.35 V can be fitted to a straight line with a slope of 3.9 (Fig. 4g). This linear feature suggests that the conduction mechanism can be attributed to a typical Schottky emission^{14,35}, which occurs due to the low injection efficiency in the presence of the large barrier between the electrodes and the active h-BAs-PVP layer^{14,28}. As thermal diffusion time increases, Ag is oxidized to Ag^+ , which diffuses through the active material along the applied electrical field, leading to a higher concentration of Ag^+ in the active layers, and some silver atoms will be deposited on the BE for the high I_{cc} . The contact with the h-BAs nanosheet or the counter electrode can reduce Ag^+ to Ag, leading to Ag filaments^{27,36}. Hence, an internal electric field is formed due to the loss of electrons accumulated in the active layer. Accordingly, the formation of the conductive paths switches the device from the HRS to the LRS. Then, the slope raised to about 2.2 as the current increased rapidly under the threshold voltage from 0.36 to 0.43 V, obeying Child's law ($I \propto V^{2.2}$) (Region B)³⁶, as shown in the inset of Fig. 4g. This process aligns with the ongoing formation of Ag filaments, which ultimately establish contact between both electrodes and establish the LRS³⁰. On the voltage backward sweep, the slope of the I - V relationship (Region D, Fig. 4h) is around 1.03, demonstrating ohmic conduction behavior³⁰. The current via the device starts to drop at a certain voltage, indicating the beginning of the dissolution of the Ag filament inside the h-BAs-PVP layer. Moreover, Ag filament paths in the h-BAs were not disconnected immediately after the device was powered off due to the insulating nature of the PVP material¹⁴. This resulted in the high conductivity and non-volatility of the devices. These findings suggest a behavior similar to the formation of conducting filaments observed in electrochemical metallization memristors³⁷.

We further use ion beam sputtering to perform depth-profiling XPS scans to analyze the change of the Ag chemical state at the top interface and inside the h-BAs-PVP layer of the devices at the ON state

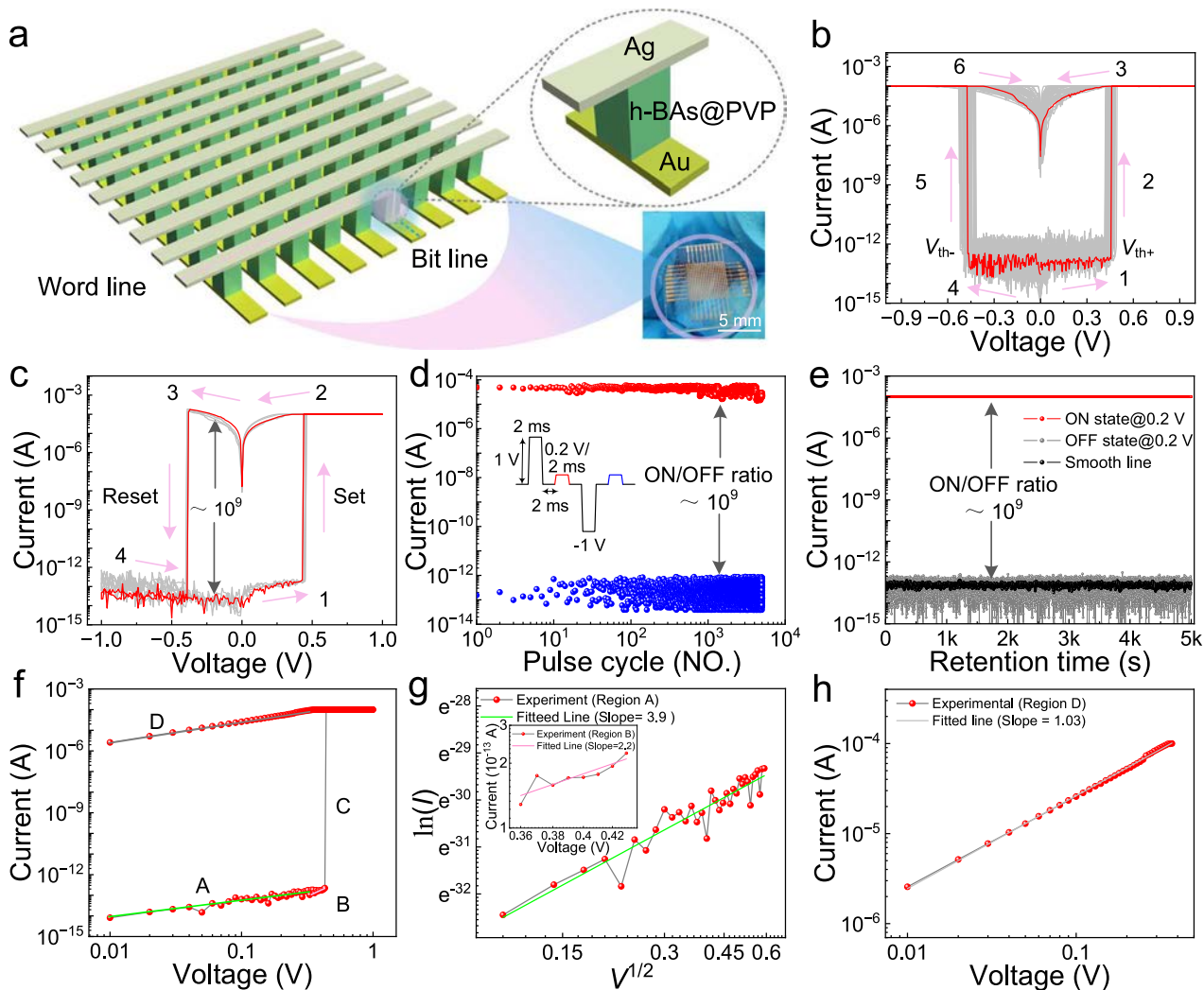


Fig. 4 | Representation and characterization of the Ag/h-BAs-polyvinylpyrrolidone (PVP)/ Au/quartz memory device. **a** Photograph and illustration of the fabricated memory device on a quartz substrate. **b** Repeatable bi-directional threshold switching I - V characteristics during 50 cycles, the positive threshold voltage (V_{th+}) and negative threshold voltage (V_{th-}) distribution is relatively narrow. **c** Repeatable bipolar memristive switching I - V curves during five cycles. **d** Pulse endurance test of the memristor showing over 5000

programming cycles. The applied set and read pulses are 1 V/2 ms and 0.2 V/2 ms, respectively. The interval between the set and read pulses is 2 ms. **e** The retentionability test of the h-BAs-based memory device in the ON and OFF states at a reading voltage of 0.2 V. **f** Typical I - V characteristics of the h-BAs-based memory device. Experimental data and fitted lines of the I - V characteristics in **g** OFF (the inset in the upper left corner is I - V characteristics under voltage from 0.36 to 0.43 V) and **h** ON state.

as shown in Supplementary Fig. 12. On the top interface of the device, Ag $3d$ core level spectra can be fitted into two components, with peaks for Ag $3d_{5/2}$ and Ag $3d_{3/2}$ located at 368.1 and 374.2 eV representing the Ag atoms (Supplementary Fig. 12a). As the sputtering time extends, the presence of Ag_xO at the Ag/h-BAs-PVP interface was examined. After extended sputtering, Ag $3d$ core level spectra can be fitted into two components, with peaks for Ag $3d_{5/2}$ and Ag $3d_{3/2}$ located at 367.5 and 373.5 eV, associated with the combined consistent with the h-BAs-PVP-Ag charge transfer, while 368.5 and 374.5 eV representing the reduced Ag atoms (Supplementary Fig. 12b, c). Further extended sputtering, there is only reduced Ag atoms can be found in the deep layer (Supplementary Fig. 12d). This observation is consistent with the general proposed mechanism for Ag-based memristors in which the h-BAs-PVP inside the active layer acts as an Ag ions reservoir and regulator of Ag conductive filaments, which output/store Ag ions under the external electric field and result in the formation/rupture of Ag filaments^{31,38}.

Furthermore, we monitored the electrical switching properties of the flexible Ag/Al₂O₃/h-BAs-PVP/Au/PET memory device, such as write cycling, retention time at room temperature, and flexibility endurance, as presented in Fig. 5. This device also shows a coexistence of both TS

and MS characteristics. In TS mode, the I - V curve of the device (Fig. 5b) displays the bi-directional TS performance over 100 cycles between the HRS (OFF state) and the LRS (ON state). The positive/negative threshold voltages are estimated by Gaussian distributions to be 0.165 ± 0.02 and -0.174 ± 0.03 V, respectively, using 100 μ A compliance current (Supplementary Fig. 13a, b). Although the resistance values of both the HRS and LRS showed slight fluctuations, an ON/OFF ratio of 10^6 was obtained without any noticeable degradation during the 100 cycles. The I - V curves are measured by changing the compliance current from 1.0×10^{-9} to 1.0×10^{-4} A by 10^{-1} A interval in the positive voltage sweep, where bipolar switching behavior is obtained at each compliance current (Supplementary Fig. 13c). The power consumption during the switching-on transition can be as low as 150 pW, that is, $P_{th+} = I_{LRS}V_{th+} = 1 \text{ nA} \times 0.15 \text{ V} = 150 \text{ pW}$. The achievement of multiple resistance states is a key performance metric for building artificial neural networks with multiple states for various applications³⁹. In MS mode, repeatable bipolar memristive switching I - V curves during 10 cycles were shown in Fig. 5c. Further measurements of the device's performance and stability were performed using rectangular voltage pulses. Switching time (t) and energy

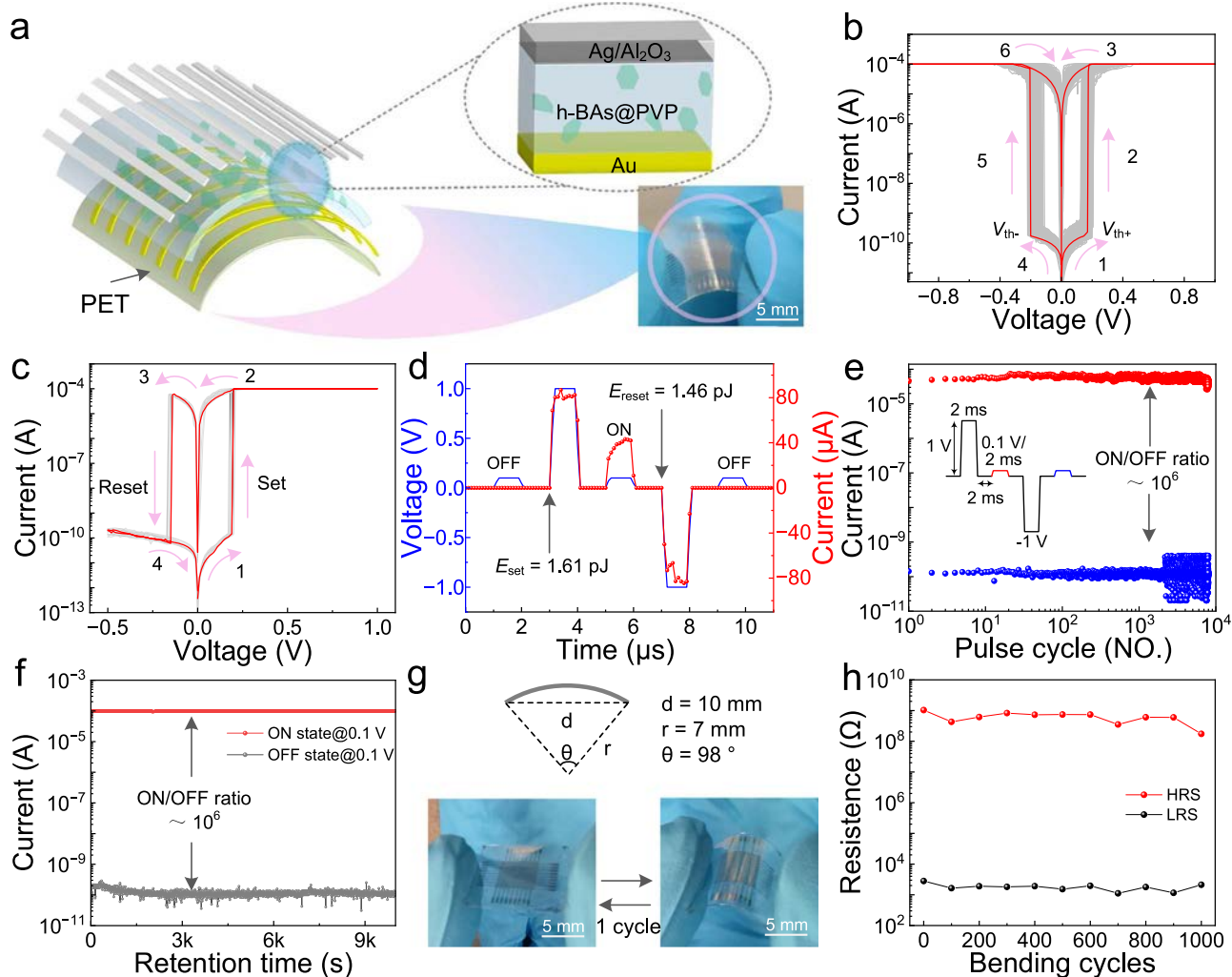


Fig. 5 | Representation and characterization of the Ag/Al₂O₃/h-BAS-PVP/Au/PET memory device. **a** Photograph and illustration of the fabricated memory device on the polyethylene terephthalate (PET) substrate. **b** Repeatability of bi-directional threshold switching I - V characteristics during 100 cycles. **c** Repeatability of bipolar memristive switching I - V curves during 10 cycles, and **d** Switching time and energy consumption of the switch by using single pulses for the set and reset processes, showing the entire set-reset cycle. **e** Pulse endurance test of $100 \times 100 \mu\text{m}$ Ag/Al₂O₃/h-BAS-PVP/Au memristor showing over 8000 programming

cycles. The applied set and read pulses are $1\text{V}/2\text{ms}$ and $0.1\text{V}/2\text{ms}$, respectively. The interval between the set and read pulses is 2ms . **f** The retention-ability test of the h-BAS-based memory device in the ON and OFF states at a reading voltage of 0.1V . **g** Photo of the slip process of the device under bending strain. The bending radius (r) is 7mm , device length while bending (d) is about 10mm , bending angle (θ) is about 98° . **h** Stability of high-resistance state (HRS) and low-resistance state (LRS) after different bending cycles.

(E) of the device can be pushed down to $t_{\text{set}} = 200\text{ns}$, $t_{\text{reset}} = 200\text{ns}$, $E_{\text{set}} = 80.3\mu\text{A} \times 0.1\text{V} \times 200\text{ns} = 1.61\text{pJ}$, and $E_{\text{reset}} = 73.1\mu\text{A} \times 0.1\text{V} \times 200\text{ns} = 1.46\text{pJ}$ (Fig. 5d). The endurance of the devices was tested at set pulses of 1V and reset pulses of -1V . The read operation was performed at 0.1V with a 2ms pulse length. The sequence of the cycles was: read, set, read, and reset. In these experiments, we demonstrated endurance better than 8000 cycles without obvious degeneration of the ON and OFF states (see Fig. 5e). Both states showed no disturbance for around $1 \times 10^4\text{s}$ (Fig. 5f). The resistance values were read out at 0.1V . To confirm the feasibility of the h-BAS-based device for flexible memory application, bending tests were carried out under repeated cycles (1000 times), as shown in Fig. 5g, h. The I - V characteristics of every 100 bends of the h-BAS-based memory device are shown in Supplementary Fig. 14. It is observed that the ON/OFF ratios did not change much (Fig. 5h) when a bending radius (r) of 7mm was applied to the devices, indicating promising bending stability and suggesting that this Ag/Al₂O₃/h-BAS-PVP/Au/PET device is mechanically robust and suitable for flexible memory application.

To assess the conduction and switching mechanisms, the I - V curves of the Ag/Al₂O₃/h-BAS-PVP/Au device were replotted in double logarithmic plots and linearly fitted for the voltage sweep region (Supplementary Fig. 15). The current conformed to the ohmic conduction characteristic ($I \propto V^{1.1}$) with a slope around 1 in the resistance transition region, indicating a small current due to the limited presence of thermally excited charge carriers in the active h-BAS-PVP layer (Supplementary Fig. 15b)³⁶. Then, the slope raised to about 2.2 as the current increased rapidly under the threshold voltage, obeying Child's law ($I \propto V^{2.2}$) (Supplementary Fig. 15c)^{35,36}. The slope increases with increasing voltage; a varying slope could indicate a varying trap density, which could be explained by the redistribution of Ag⁺ ions. The inserting Al₂O₃ layer is found to accelerate the oxidation of silver into silver ions, allowing the silver ions to diffuse rapidly in the h-BAS-PVP layer, which makes the leakage current of the device higher but relatively less volatile, and the set voltage also becomes lower. When the Ag⁺ ions contact with the h-BAS nanosheet or the counter electrode, Ag⁺ are reduced to Ag, which leads to the formation of Ag filaments, resulting in exhibiting an ohmic behavior ($I \propto V^{1.1}$) in the LRS

(Supplementary Fig. 15d). The linear fit reveals that the device of HRS is dominated by the space charge limited conduction mechanism, while LRS conforms to ohmic conduction^{36,40,41}. We further perform depth-profiling XPS scans to analyze the change of the Ag chemical state at the top interface and inside the h-BAs-PVP layer of the devices at the ON state, as shown in Supplementary Fig. 16. Conductive silver filaments were found at different depths of the device, which is the same as that of the device on the quartz substrate. The diffusion of silver penetrates the Al₂O₃ and h-BAs-PVP layer to form conductive filaments. In addition, we also used electrodes of different sizes to make devices of different cell areas (10 × 10, 20 × 20, 50 × 50, 200 × 200 μm²), tested the *I*-*V* curve without current compliance, and compared the current changes under a read voltage of 0.1 V in the ON and OFF states (Supplementary Fig. 17). It can be found that the larger the device area, the larger the current that can be achieved in the ON state, but the current in the OFF state has almost no change. This is mainly because the larger the device area, the more silver conductive filaments can be formed, thereby increasing the current in the LRS^{38,42}. It was further experimentally proven that the mechanism of the memristor effect is an Ag ions reservoir and regulator of Ag conductive filaments at the h-BAs-PVP active layer.

We then compared our device with high-performing devices from other nanomaterials, such as h-BN, borophene, MoS₂, and other typical 2D materials (Supplementary Table 1)^{28,37,39,40,42–53}. The results indicate that the h-BAs-based memristor has an ultrahigh switching window (>10⁹) and power consumption (<4.65 pJ), and these properties are comparable to the best reported III-V memristor materials, h-BN³⁹, and exceed those of most other common 2D materials, demonstrating that it has great potential applications in advanced memory devices with low energy consumption.

Discussion

In summary, we have successfully prepared ultrathin crystalline semiconducting hexagonal BAs nanosheets through an in situ thermal decomposition and combination process. The obtained h-BAs nanosheet is a promising 2D material with a lateral size exceeding 1 μm and a thickness of ~2.75 nm. They show robust stability in strong acid and base solvents during the cleaning and purification process. Furthermore, as a proof-of-concept application, a h-BAs-based memory device was fabricated, which showed a memory effect with a high ON/OFF current ratio of more than 10⁹ and ultra-low-power consumption (<4.65 pJ) with good stability. It is believed that the promising h-BAsNs might open up more advanced applications in electronics, photodetectors, and sensing.

Methods

Material synthesis

All the chemicals, including arsenic (As, ≥99.999%), sodium borohydride (NaBH₄, 99%), hydrochloric acid (HCl, 37%), and PVPy (*M_w* ≈ 1,300,000), were purchased from Sigma-Aldrich and used without further processing. Ultrapure deionized (DI) water was used for all solution preparations. Sodium borohydride and arsenic were mixed in a molar ratio of 1:2 and grounded in an agate mortar for half an hour in a glove box. Then, 30 mg was placed in a special quartz boat and reacted in a tubular furnace in a low-pressure hydrogen atmosphere. The h-BAs were prepared by an in situ chemical reaction of sodium borohydride with elemental arsenic at 650 °C for 30 min. The programming temperature curve is shown in Supplementary Fig. 1. After the reaction, the powder was soaked in 5% hydrochloric acid for 10 min, ultrasonicated in deionized water for 30 min, and then the upper dispersion was centrifuged. The precipitate obtained by centrifugation was washed with deionized water and alcohol and centrifuged three times to obtain hexagonal BAs nanosheets.

Material characterizations

SEM images were obtained with the FEI Quanta 450 FESEM analysis system. AFM (Bruker Multimode 8 Nanoscope) was used to get the thickness profile of the as-synthesized h-BAs nanosheets. TEM images and SAED patterns were performed on an FEI Talos F200S field emission transmission electron microscope at an accelerating voltage of 200 kV. EDS mappings were carried out on a Thermo Fisher Scientific Spectra 300 S/TEM at an accelerating voltage of 300 kV. Chemical states, elemental composition analyses, and depth-profiling XPS of the devices were performed by XPS (ESCALAB 250Xi, Thermo Fisher Scientific Inc.) with a focused monochromatized Al Kα irradiation. XRD patterns were collected on a Rigaku SmartLab high-resolution X-ray diffractometer. Raman measurement was carried out on a WITec alpha300 R Raman System with a laser wavelength of 532 nm. ATR-FTIR spectroscopy was recorded on a PerkinElmer FTIR Spectrometer. At room temperature, UV-vis absorption spectra were recorded on a Hitachi UH4150 UV-VIS-NIR Spectrophotometer.

Device fabrication

A two-terminal RRAM with a sandwich structure was fabricated. An Au film with a thickness of 40 nm was deposited by thermal evaporation through a shadow mask on the quartz or flexible PET substrate as the BE. The mixture of ethanol solution of PVPy (20 mg mL⁻¹, *M_w* = 1,300,000), containing 10 wt% (relative to PVPy) of the h-BAs nanosheets, was spin-coated on the Au-coated substrate at a speed of 1500 rpm for 60 s, to form the electroactive layer, and was annealed at 70 °C for 30 min. Finally, a 40 nm thick Ag film was deposited on the active layer via thermal evaporation through a mask as the TE. The difference is that before evaporating the silver electrode on the PET substrate, a 5 nm thick Al₂O₃ layer is first evaporated by the electron beam. The width of both the Au BE and Ag TE is 0.2 mm, and one single device has a size of 0.04 mm² and forms 18 × 18 cross-bar structures on the substrate. The electrical performance of the device was recorded by the Agilent 4155 C semiconductor analyzer with a standard electrical probe station. A 4200-SCS Keithley semiconductor analyzer combined with the probe station is used for pulse measurements.

Theoretical computation details

The first principal calculation based on DFT is realized by the Vienna Ab-initio Simulation Package code^{54,55} with the full-potential projected augmented wave formalism⁵⁶. The generalized gradient approximation under the Perdew–Burke–Ernzerhof (PBE) formalism was applied to describe exchange correlation⁵⁷. A vacuum layer of 15 Å is applied to avoid perturbations from neighboring layers. The cutoff energy for the plane-wave expansion is set to 450 eV. A convergence criterion of 10⁻⁵ eV is set for self-consistency, and the structure is relaxed until the maximum stress on each atom is lower than 0.01 eV/Å. The Γ -centered K-point mesh of 5 × 5 × 1 is used for the DOS calculation. Moreover, the PBE0 hybrid functional was used to calculate the band structure of h-BAs. For the decomposition of sodium borohydride and formation of BAs, the basic set of the double numerical plus polarization and the DFT-D method for van der Waals dispersion corrections with the Grimme scheme were employed to describe the way of occupied molecular orbital expansion and to measure electrostatic interactions accurately, respectively. The convergence criteria for electronic energy, max displacement, and max force on each atom were 1.0 × 10⁻⁵ Ha/atom, 0.005 Å, and 0.002 Ha Å⁻¹, respectively.

Data availability

The Source Data underlying the figures of this study are available with the paper. All raw data generated during the current study are available from the corresponding authors upon request. Source data are provided with this paper.

References

1. Kang, J. S., Li, M., Wu, H. A., Nguyen, H. & Hu, Y. J. Experimental observation of high thermal conductivity in boron arsenide. *Science* **361**, 575–578 (2018).
2. Li, S. et al. High thermal conductivity in cubic boron arsenide crystals. *Science* **361**, 579–581 (2018).
3. Yue, S. et al. High ambipolar mobility in cubic boron arsenide revealed by transient reflectivity microscopy. *Science* **377**, 433–436 (2022).
4. Li, S. et al. Anomalous thermal transport under high pressure in boron arsenide. *Nature* **612**, 459–464 (2022).
5. Choudhry, U. et al. Persistent hot carrier diffusion in boron arsenide single crystals imaged by ultrafast electron microscopy. *Matter* **6**, 206–216 (2023).
6. Lindsay, L., Broido, D. A. & Reinecke, T. L. First-principles determination of ultrahigh thermal conductivity of boron arsenide: a competitor for diamond? *Phys. Rev. Lett.* **111**, 025901 (2013).
7. Tian, F. & Ren, Z. High thermal conductivity in boron arsenide: from prediction to reality. *Angew. Chem. Int. Ed.* **58**, 5824–5831 (2019).
8. Zhang, J., Liu, H., Gao, Y., Xia, X. & Huang, Z. The sp^2 character of new two-dimensional AsB with tunable electronic properties predicted by theoretical studies. *Phys. Chem. Chem. Phys.* **21**, 20981–20987 (2019).
9. Hu, Y. et al. High thermal conductivity driven by the unusual phonon relaxation time platform in 2D monolayer boron arsenide. *RSC Adv.* **10**, 25305–25310 (2020).
10. Manoharan, K. & Subramanian, V. Exploring multifunctional applications of hexagonal boron arsenide sheet: a DFT Study. *ACS Omega* **3**, 9533–9543 (2018).
11. Cui, Y., Qin, Z., Wu, H., Li, M. & Hu, Y. Flexible thermal interface based on self-assembled boron arsenide for high-performance thermal management. *Nat. Commun.* **12**, 1284 (2021).
12. Kaneti, Y. V. et al. Borophene: Two-dimensional boron monolayer: synthesis, properties, and potential applications. *Chem. Rev.* **122**, 1000–1051 (2022).
13. Awasthi, A. & Subhash, G. Deformation behavior and amorphization in icosahedral boron-rich ceramics. *Prog. Mater. Sci.* **112**, 100664 (2020).
14. Hou, C. et al. Ultrastable crystalline semiconducting hydrogenated borophene. *Angew. Chem. Int. Ed.* **59**, 10819–10825 (2020).
15. Wang, S. et al. Synthesis and characterization of a p-type boron arsenide photoelectrode. *J. Am. Chem. Soc.* **134**, 11056–11059 (2012).
16. Kirillov, S. A. & Yannopoulos, S. N. Vibrational dynamics as an indicator of short-time interactions in glass-forming liquids and their possible relation to cooperativity. *J. Chem. Phys.* **117**, 1220–1230 (2002).
17. Beard, A. M. et al. Thermal dehydration and vibrational spectra of hydrated sodium metaborates. *Ind. Eng. Chem. Res.* **50**, 7746–7752 (2011).
18. Whiteley, C. E. et al. Semiconducting icosahedral boron arsenide crystal growth for neutron detection. *J. Cryst. Growth* **318**, 553–557 (2011).
19. Huang, C. J. et al. Stable colloidal boron nitride nanosheet dispersion and its potential application in catalysis. *J. Mater. Chem. A* **1**, 12192–12197 (2013).
20. Zarechnaya, E. Y. et al. Superhard semiconducting optically transparent high-pressure phase of boron. *Phys. Rev. Lett.* **102**, 185501 (2009).
21. Wang, Y. et al. An efficient boron source activation strategy for the low-temperature synthesis of boron nitride nanotubes. *Nano Micro Lett.* **17**, 1521–1525 (2025).
22. Khossossi, N. et al. Ab initio study of a 2D h-BAs monolayer: a promising anode material for alkali-metal ion batteries. *Phys. Chem. Chem. Phys.* **21**, 18328–18337 (2019).
23. Er, S., de Wijs, G. A. & Brocks, G. DFT study of planar boron sheets: a new template for hydrogen storage. *J. Phys. Chem. C* **113**, 18962–18967 (2009).
24. Martelli, P. et al. Stability and decomposition of NaBH_4 . *J. Phys. Chem. C* **114**, 7173–7177 (2010).
25. Grochala, W. & Edwards, P. P. Thermal decomposition of the non-interstitial hydrides for the storage and production of hydrogen. *Chem. Rev.* **104**, 1283–1315 (2004).
26. Ouyang, J. Y., Chu, C. W., Szmanda, C. R., Ma, L. P. & Yang, Y. Programmable polymer thin film and non-volatile memory device. *Nat. Mater.* **3**, 918–922 (2004).
27. Fu, T. D. et al. Bioinspired bio-voltage memristors. *Nat. Commun.* **11**, 1861 (2020).
28. Zhang, X. et al. Black phosphorus quantum dots. *Angew. Chem. Int. Ed.* **54**, 3653–3657 (2015).
29. Liu, J. et al. Preparation of MoS_2 -polyvinylpyrrolidone nanocomposites for flexible nonvolatile rewritable memory devices with reduced graphene oxide electrodes. *Small* **8**, 3517–3522 (2012).
30. Chae, B. G. et al. Nanometer-scale phase transformation determines threshold and memory switching mechanism. *Adv. Mater.* **29**, 1701752 (2017).
31. Wang, Z. R. et al. Memristors with diffusive dynamics as synaptic emulators for neuromorphic computing. *Nat. Mater.* **16**, 101–108 (2017).
32. Lanza, M. et al. Standards for the characterization of endurance in resistive switching devices. *ACS Nano* **15**, 17214–17231 (2021).
33. Zhu, K. C. et al. Hybrid 2D-CMOS microchips for memristive applications. *Nature* **618**, 57–62 (2023).
34. Yang, Y. C. et al. Electrochemical dynamics of nanoscale metallic inclusions in dielectrics. *Nat. Commun.* **5**, 4232 (2014).
35. Warren, A. C. Reversible thermal breakdown as a switching mechanism in chalcogenide glasses. *IEEE Trans. Electron Devices* **20**, 123–131 (1973).
36. Liu, Y. et al. Inkjet-printed metal-organic frameworks for non-volatile memory devices suitable for printed RRAM. *Adv. Funct. Mater.* **35**, 2412372 (2025).
37. Pazos, S. et al. Memristive circuits based on multilayer hexagonal boron nitride for millimetre-wave radiofrequency applications. *Nat. Electron.* **7**, 557–566 (2024).
38. Zhang, T. et al. Rationally designing high-performance versatile organic memristors through molecule-mediated ion movements. *Adv. Mater.* **35**, 2302863 (2023).
39. Li, Y. et al. Ag-doped non-imperfection-enabled uniform memristive neuromorphic device based on van der Waals indium phosphorus sulfide. *Sci. Adv.* **10**, eadk9474 (2024).
40. Shi, Y. et al. Electronic synapses made of layered two-dimensional materials. *Nat. Electron.* **1**, 458–465 (2018).
41. Lanza, M. et al. Memristive technologies for data storage, computation, encryption, and radio-frequency communication. *Science* **376**, 1066–1079 (2022).
42. Tang, B. et al. Wafer-scale solution-processed 2D material analog resistive memory array for memory-based computing. *Nat. Commun.* **13**, 3037 (2022).
43. Nibhanupudi, S. S. T. et al. Ultra-fast switching memristors based on two-dimensional materials. *Nat. Commun.* **15**, 2334 (2024).
44. Yen, M. C. et al. All-inorganic perovskite quantum dot light-emitting memories. *Nat. Commun.* **12**, 4460 (2021).
45. Ahmed, T. et al. Mixed ionic-electronic charge transport in layered black-phosphorus for low-power memory. *Adv. Funct. Mater.* **32**, 2107068 (2021).
46. Wang, Y. et al. High on/off ratio black phosphorus based memristor with ultra-thin phosphorus oxide layer. *Appl. Phys. Lett.* **115**, 193503 (2019).
47. Sun, L. et al. Self-selective van der Waals heterostructures for large-scale memory array. *Nat. Commun.* **10**, 3161 (2019).

48. Chen, S. et al. Wafer-scale integration of two-dimensional materials in high-density memristive crossbar arrays for artificial neural networks. *Nat. Electron.* **3**, 638–645 (2020).
49. Yang, S. J. et al. Volatile and nonvolatile resistive switching coexistence in conductive point hexagonal boron nitride monolayer. *ACS Nano* **18**, 3313–3322 (2024).
50. Hu, J. Y. et al. Self-compliant, variation-suppressed memristor implemented with carbon nanotube/hBN/silver nanowire cross-point structure. *Adv. Funct. Mater.* 2424131 <https://doi.org/10.1002/adfm.202424131> (2025).
51. Sivan, M. et al. All WSe₂ 1T1R resistive RAM cell for future monolithic 3D embedded memory integration. *Nat. Commun.* **10**, 5201 (2019).
52. Xu, R. J. et al. Vertical MoS₂ double-layer memristor with electrochemical metallization as an atomic-scale synapse with switching thresholds approaching 100 mV. *Nano Lett.* **19**, 2411–2417 (2019).
53. Wu, Z. T. et al. Synthesis and anisotropic memristive behavior of borophene nanosheets. *Angew. Chem. Int. Ed.* **64**, e202416041 (2025).
54. Kresse, G. & Furthmüller, J. Efficient iterative schemes for ab initio total-energy calculations using a plane-wave basis set. *Phys. Rev. B* **54**, 11169–11186 (1996).
55. Perdew, J. P., Burke, K. & Ernzerhof, M. Generalized gradient approximation made simple. *Phys. Rev. Lett.* **78**, 1396–1396 (1997).
56. Blochl, P. E. Projector augmented-wave method. *Phys. Rev. B* **50**, 17953–17979 (1994).
57. Kresse, G. & Joubert, D. From ultrasoft pseudopotentials to the projector augmented-wave method. *Phys. Rev. B* **59**, 1758–1775 (1999).

Acknowledgements

This work is supported by a fellowship award from the Research Grants Council of the Hong Kong Special Administrative Region, China (CityURFS2021-1S04), the Innovation and Technology Fund (MHP/O44/23) from the Innovation and Technology Commission of the Hong Kong Special Administrative Region, China, the Science Technology and Innovation Committee of Shenzhen Municipality (Project No. JCYJ20230807114910021), and Guangdong Basic and Applied Basic Research Fund (Project no. 2024A1515011922).

Author contributions

Z.H.W. and J.C.H. conceived and initiated the project. Z.H.W. prepared materials and fabricated devices, and performed analysis. B.X.G. contributed to the XPS test. Y.X.Z. and W.J.W. performed the AFM measurements. S.P.Y., Q.Q., D.Y., Y.S., D.C., and Z.C.X. performed part of the

analysis. M.Y., H.S., D.J.L., P.S.X., W.J.W., and B.W.L. helped with the electrical measurement. Y.X.Z. performed the DFT calculation. Z.H.W. and J.C.H. wrote the initial manuscript. All authors contributed to the final manuscript and approved the submission.

Competing interests

The authors declare no competing interests.

Additional information

Supplementary information The online version contains supplementary material available at <https://doi.org/10.1038/s41467-025-60038-3>.

Correspondence and requests for materials should be addressed to Johnny C. Ho.

Peer review information *Nature Communications* thanks Xinfeng Liu, Kaichen Zhu, and the other, anonymous, reviewer(s) for their contribution to the peer review of this work. A peer review file is available.

Reprints and permissions information is available at <http://www.nature.com/reprints>

Publisher's note Springer Nature remains neutral with regard to jurisdictional claims in published maps and institutional affiliations.

Open Access This article is licensed under a Creative Commons Attribution-NonCommercial-NoDerivatives 4.0 International License, which permits any non-commercial use, sharing, distribution and reproduction in any medium or format, as long as you give appropriate credit to the original author(s) and the source, provide a link to the Creative Commons licence, and indicate if you modified the licensed material. You do not have permission under this licence to share adapted material derived from this article or parts of it. The images or other third party material in this article are included in the article's Creative Commons licence, unless indicated otherwise in a credit line to the material. If material is not included in the article's Creative Commons licence and your intended use is not permitted by statutory regulation or exceeds the permitted use, you will need to obtain permission directly from the copyright holder. To view a copy of this licence, visit <http://creativecommons.org/licenses/by-nc-nd/4.0/>.

© The Author(s) 2025